Petroleum Science 20 (2023) 2521–2530

Contents lists available at ScienceDirect

Petroleum Science

journal homepage: www.keaipublishing.com/en/journals/petroleum-science

Original Paper

Optimization of dendritic TS-1/Silica micro–mesoporous composites for efficient hydrodesulfurization of dibenzothiophene and 4,6-dimethyldibenzothiophene

Cheng-Kun Xiao [a, 1], Yu-Tong Zou [a, 1], Dong-Ze Li [a], En-Hua Wang [a], Ao-Cheng Wang [a], Dao-Wei Gao [b], Ai-Jun Duan [a], Peng Zheng [a, **], Xi-Long Wang [a, *]

[a] State Key Laboratory of Heavy Oil Processing, China University of Petroleum, Beijing, 102249, China
[b] School of Chemistry and Chemical Engineering, University of Jinan, Jinan, Shandong, 250022, China

ARTICLE INFO

Article history:
Received 13 February 2023
Received in revised form
8 April 2023
Accepted 3 July 2023
Available online 4 July 2023

Edited by Jia-Jia Fei

Keywords:
Dendritic TS-1-DMSNs composites
NiMo/TD catalysts
Dibenzothiophene
4,6-Dimethyldibenzothiophene
Hydrodesulfurization

ABSTRACT

A novel composite material (TD) composed of TS-1 microcrystalline and dendritic mesoporous silica nanospheres (DMSNs) was successfully prepared. The TD composite material had open pore structure and large specific surface area, which was conducive to the mass transfer of reactants and products. The Ti element in TS-1 could be used as an electron assistant, and the spillover d-electrons were conducive to the improvement of the sulfidation and dispersion of MoS_2, thereby forming more type II MoS_2 active phases. The incorporation of Ti could bring more Brønsted (B) and Lewis (L) acid, which was conducive to the hydrogenation pathway (HYD) selectivity (41.2%) of dibenzothiophene (DBT) hydrodesulfurization (HDS) and isomerization (ISO) route selectivity (21.9%) of 4,6-dimethyldibenzothiophene (4,6-DMDBT) HDS, thus improve the HDS activity of DBT and 4,6-DMDBT. NiMo/TD-70 (Aging temperature = 70 °C) had the best HDS activities of DBT (99.0%) and 4,6-DMDBT (93.7%) due to its large open pore structure, good acidity, suitable metal-support interaction (MSI) and perfect dispersion of the metallic active sites.

1. Introduction

Nowadays, with the increasing environmental awareness and the stringent laws and regulations of fuels, how to produce ultra-low sulfur fuel has become a hot spot (Duan et al., 2015a, b; Lei et al., 2015; Shan et al., 2015; Zhou et al., 2017). In particular, it is very important to remove macromolecular sulfides such as DBT and 4,6-DMDBT in oil to improve fuel quality and reduce environmental pollution (Ho and Mcconnachie, 2011; Liang et al., 2018; Song et al., 2014; Wang et al., 2017a, b). HDS is one of the most widely used technologies for the production of clean oil products, and the hydrofining catalyst is the core of the HDS technology (Lei et al., 2012; Zhou et al., 2018). Therefore, the research and development of new supports and catalysts has become the focus of the petroleum industry (Du et al., 2017; Hu et al., 2020; Wang et al., 2020a, b).

The traditional HDS catalysts using alumina as the support has gradually been difficult to meet the demand of ultra-deep desulfurization owing to its low specific surface area, disordered pore properties and high MSI (Shan et al., 2016; Haandel et al., 2015; Han et al., 2016). Recently, a new type of DMSNs has attracted widespread attention (Hu et al., 2020; Wang et al., 2020a, b), which has an open three-dimensional dendritic pore structure, growing from the center to the outer surface in a pleat shape. The large specific surface area of DMSNs can disperse uniformly the active metal without blocking the pores. The open pore structure can reduce diffusion resistance and make reactants and active metal easier contact (Huang et al., 2014; Shen et al., 2014; Wu et al., 2011; Yu et al., 2014). However, DMSNs material also has certain disadvantages, the pure silica composition of DMSNs determined its low acidity and MSI, which limited its application in HDS reactions (Wang et al., 2020a, b). Many researchers use a micro-mesoporous composite method to prepare composite materials like ZSM-5, β, TS-1 and other zeolites are composited with pure silica-based

* Corresponding author.
** Corresponding author.
E-mail addresses: zhengpengc@126.com (P. Zheng), wxl@cup.edu.cn (X.-L. Wang).
[1] Cheng-Kun Xiao and Yu-Tong Zou contributed equally to this work.

https://doi.org/10.1016/j.petsci.2023.07.004

materials (Li et al., 2017; Moliner et al., 2015; Nikolla et al., 2011; Sun et al., 2009), which not only bring more acidity and hydrothermal stability to the composite materials, but also adjust MSI while maintaining the large pore size of the mesoporous structure, so that the composites have both advantages of microporous and mesoporous materials (Wang et al., 2018a, b; Zhang et al., 2010). TS-1 zeolite has good acid properties, and Ti element of TS-1 zeolite as an electronic promoter can improve the sulfidation of active metal, thus improving the HDS activity of catalyst (Li et al., 2017; Xiao et al., 2018).

In the present work, TD-*x* composites with different morphologies and acidity and the corresponding NiMo/TD-*x* series catalysts were prepared for DBT and 4,6-DMDBT HDS. Some characterization methods were used to this research. It was found that NiMo/TD-70 catalyst had the optimal hydrodesulfurization activities of DBT (99.0%) and 4,6-DMDBT (93.7%) due to its large open pore structure, good acidity, suitable MSI and perfect dispersion of the metallic active sites.

2. Experimental

2.1. Preparation of supports and catalysts

TS-1 microcrystalline (Si/Ti = 33) was prepared by the method described in the literature (Wang et al., 2020a, b). Firstly, 40 g silicon source (tetraethyl orthosilicate, 98%) and 1.98 g titanium source (tetrabutyl titanate, ≥99.0%) were dropped into the deionized water containing Tetrapropylammonium hydroxide (46.72 g, 25 wt%) respectively, stirring continuously for 1 h. Then, 48 g isopropanol (≥99.7%) was added to the above system after stirring for 3 h under 70 °C water bath. After hydrothermal crystallization at 170 °C for 96 h, the TS-1 precursor seed powder was synthesized by filtration and drying.

The TD micro-mesoporous composites were prepared by the follows: 0.82 g triethanolamine (≥99.0%), 5.02 g cetyltrimethylammonium bromide (99%) and 4.56 g sodium salicylate (99%) were added into water at different water bath temperatures (40, 60, 70, 80 and 90 °C) and kept stirring until the solution was homogeneous. Then, Tetraethyl orthosilicate was added slowly and kept stirring, then 2 g TS-1 crystal seed were added. After 2 h, the mixed solution was crystallized at 100 °C for 4 h. Finally, TD-*x* (*x* = 40, 60, 70, 80 and 90) micro-mesoporous composites were synthesized.

The series NiMo/TD-*x* catalysts and commercial NiMo/Al_2O_3 catalyst introduced in Supporting Information were prepared with 15.5 wt% MoO_3 and 3.5 wt% NiO, respectively.

2.2. Characterization and catalytic performance evaluation

The characterization methods and calculation methods (Duan et al., 2015a, b; Li et al., 2018; Wang et al., 2016, 2018) were introduced in Supporting Information.

3. Results

3.1. Structure properties of supports

The wide-angle X-ray diffraction (XRD) patterns of TS-1 and series TD-*x* supports are shown in Fig. 1. The characteristic peaks belonging to MFI structure are displayed at 2θ = 7.8°, 8.8°, 23.2°, 23.8° and 24.3°, which are indicative five characteristic reflections of TS-1 zeolite (Lee et al., 2011). Compared with TS-1, the peak intensities of series TD supports are significantly reduced, indicating that TS-1 in the composites are mainly the primary or secondary unit structures.

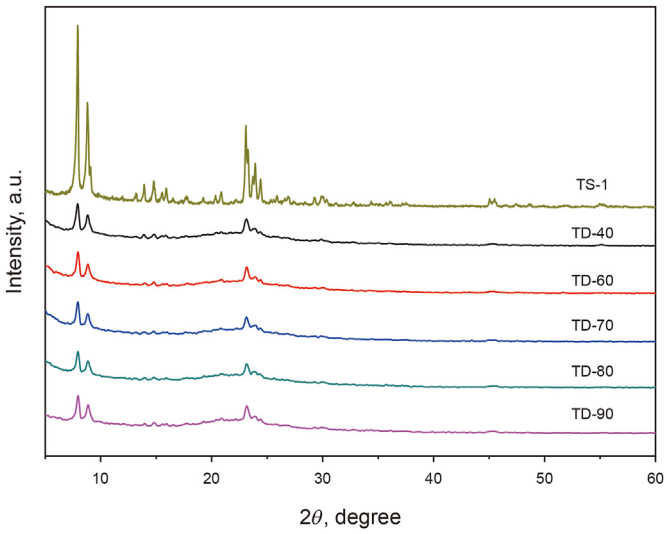

Fig. 1. Wide-angle XRD patterns of TS-1 and TD-*x* supports.

The ^{29}Si magic angle spinning nuclear magnetic resonance (^{29}Si MAS NMR) patterns of DMSNs and TD-x supports are shown in Fig. 2. There are three peaks at $\delta = -112$, -102 and -90 nm labeled Q4, Q3 and Q2 assigned to $Si(-O-)_4$, $SiOH(-O-)_3$ and $SiOH_2(-O-)_2$, respectively (Hamdy et al., 2010; Wang et al., 2020a). The peaks belong to $SiOH(-O-)_3$ and $SiOH_2(-O-)_2$ in series TD-*x* supports are obviously weaker than that in DMSNs, which indicates that the Si and Ti atoms of TS-1 replace the hydroxyl group of DMSNs and bind with Si–O–Si and Si–O–Ti.

The fourier transform infrared spectroscopy (FTIR) patterns of TS-1 and series TD-*x* supports are shown in Fig. 3. The characteristic peaks at 808 and 1068 cm^{-1} are attributed to the symmetric and asymmetric stretching vibrations of Si–O–Si band, respectively. The characteristic peaks at 966 and 1640 cm^{-1} are attributed to silanol (Hamdy et al., 2010; Zhao and Yu, 2006). The peaks at 966 and 808 cm^{-1} of TD series supports have obvious red shifts compared with TS-1. The shift peak at 966 cm^{-1} is mainly due to the existence of more Si–O–Ti band, the other shift peak at 808 cm^{-1} is the result of the interaction of Si–O–Si and Ti–O–Ti

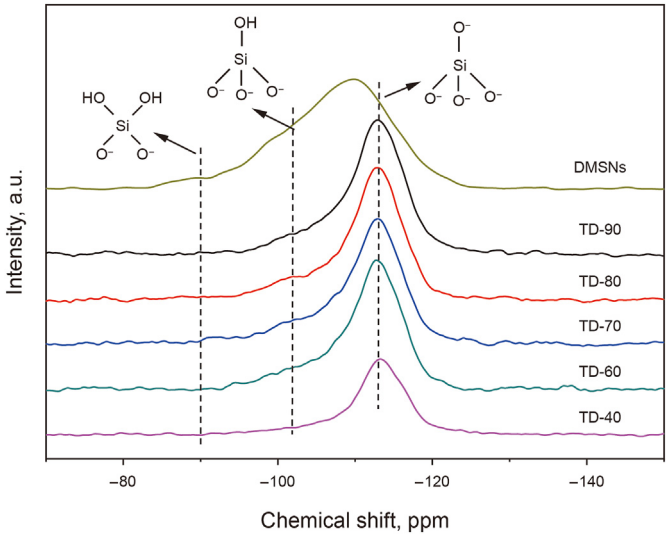

Fig. 2. ^{29}Si NMR patterns of TD-*x* supports.

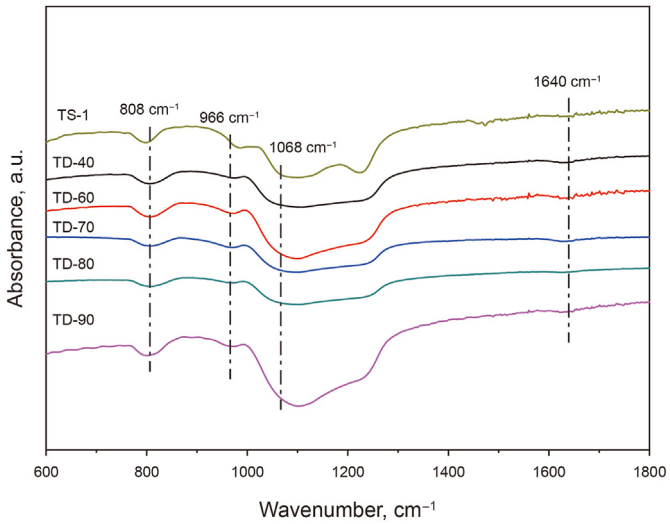

Fig. 3. FTIR patterns of TS-1and TD-*x* supports.

bonds (Zhao and Yu, 2006). These features indicate that TS-1 and DMSNs are bound by chemical bonds, which is correspond to Si NMR results.

As can be seen from Fig. 4, the series TD-*x* supports display type-IV isotherms and H3 hysteresis loop, which proves that TD-*x* supports have typical mesoporous structure (Ma et al., 2019; Wu et al., 2014). The hysteresis loop becomes steep firstly and then flat with the increasing of aging temperatures, indicating that its pore volume increases firstly and then diminishes. The TD-*x* series supports display a large specific surface area (234–463 m^2/g), pore volume (0.7–1.61 cm^3/g) and pore diameter (10.4–16.6 nm) (Table 1). When the aging temperature is 60 °C, TD-60 support shows the maximum.

3.2. Morphological features of supports

Figs. 5 and 6 shows the scanning electron microscopy (SEM) and transmission electron microscopy (TEM) images of TS-1 and series TD-*x* supports. The images show that TD-*x* supports are composed of nanofibers growing from the center to the periphery with wrinkled surfaces. This unique structure provides a larger accessible area and open pore structure, which is more beneficial to the dispersion of Ni and Mo as well as the diffusion of reactants and product molecules. The supports prepared at the aging temperature of 60–80 °C are more uniform.

The distribution state of TS-1 in TD-*x* supports are performed by the HADDF-STEM and EDS elemental mapping shown in Fig. 6. The uniform distribution of Ti elements indicates that TS-1 has successfully entered the DMSNs skeleton.

Table 1
Textural properties of TD-*x* supports.

Samples	S_{BET}, $m^2\ g^{-1}$	V_{mes}, $cm^3\ g^{-1}$	D_{BJH}, nm
TD-40	373	0.86	10.4
TD-60	463	1.61	16.6
TD-70	385	1.24	15.3
TD-80	340	1.23	16.0
TD-90	234	0.71	15.3

3.3. Oxidation state characterization of catalysts

Fig. 7 shows the Raman spectra of series oxide catalysts to observe the chemical state of NiMo active phase. There are five obvious peaks located at 955, 908, 820, 710 and 325 cm^{-1}, respectively. The characteristic peaks at 325 and 820 cm^{-1} are due to the four-coordinated Mo species (Salerno et al., 2004; Xiao et al., 2021). The peaks at 908 and 710 cm^{-1} are assigned to α-$NiMoO_4$ (Salerno et al., 2004; Xiao et al., 2021), which is considered as the precursor of NiMoS–I active phase in HDS reaction (Liu et al., 2020; Zhou et al., 2014). The peaks at 955 cm^{-1} owes to the polymolybdate species, like $Mo_7O_{24}^{6-}$ or $Mo_8O_{26}^{4-}$ (Mestl and Srinivasan, 1998; Parola et al., 2002). The polymolybdate species are the products of suitable MSI, which are easy to reduced and sulfurized to NiMoS– II active phase and more conducive to HDS reaction (Badoga et al., 2012). NiMo/TD-70 catalyst shows the highest peak strength.

The acidic properties of the catalysts analyzed by pyridine adsorption FTIR (Py-FTIR) spectra are shown in Fig. 8. Fig. 8(a) and (b) are the results of the series catalysts corresponded to total acids (B and L acidities), medium and strong acids, respectively (Lee et al., 2011; Wang et al., 2018a, b). It can be seen from the specific values in Table 2, NiMo/TD-70 catalyst presents the largest amount of B and L acids and B/L acid ratio.

3.4. Sulfide state characterization of catalysts

High-resolution transmission electron microscopy (HRTEM) is performed to characteristic the dispersion and morphology of MoS_2 active phase, the lengths and stacking layers of MoS_2 of sulfurized catalysts are shown in Fig. 9. Note that MoS_2 particles are uniformly dispersed on the catalysts. In order to make a more intuitive comparison of the distribution of MoS_2 active phase, the average length (L_{av}) and average stacking layers (S_{av}) are calculated by counting more than 300 MoS_2 slabs.

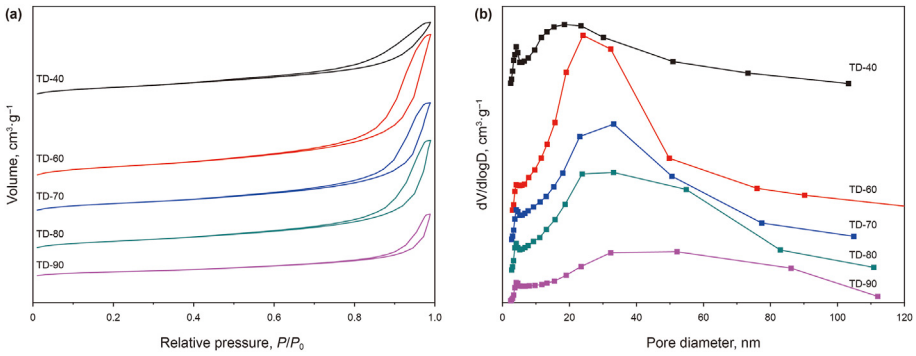

Fig. 4. N_2 physisorption isotherms (**a**) and pore size distribution patterns(**b**) of TD-*x* supports

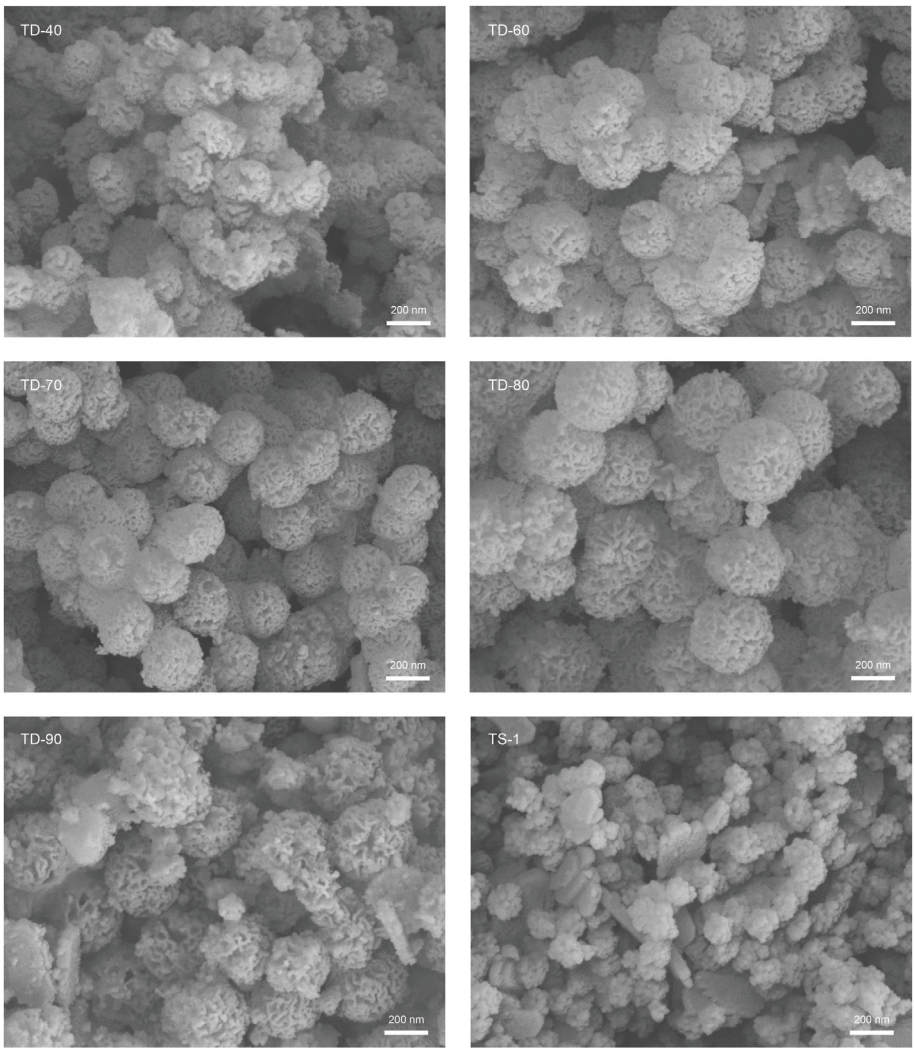

Fig. 5. SEM images of TS-1 and TD-*x* supports.

The statistic values are listed in Table 3. The NiMo/TD-70 catalyst shows a comparatively low average stacking lengths and suitable stacking layers. Additionally, f_{Mo} values present the tendency of NiMo/TD-70>NiMo/TD-80 = NiMo/TD-60>NiMo/TD-40>NiMo/TD-90, indicating that NiMo/TD-70 displays the highest dispersion degree of MoS_2 slabs. Based on the above data, it can be found that the lower stacking lengths and more moderate stacking layers promote a good dispersion of MoS_2 particles, forming more "Ni-Mo-S-II" active phases (Bouwens et al., 1994; Liu et al., 2020; Prins et al., 1989).

The sulfurization degree of catalysts is closely related to the HDS activity of sulfur-containing compounds. X-ray photoelectron spectroscopy (XPS) characterization methods are used to investigate the valent state, type and relative content of the catalyst active phase, and the specific Mo 3d XPS spectra results are exhibited in Fig. 10. As can be seen, seven characteristic peaks fitting in the XPS spectrum were assigned to Mo (Mo^{4+}, Mo^{5+} and Mo^{6+}) species and S phase (Wang et al., 2017a) and the XPS fitting standards were described in our previous work (Wang et al., 2020a, b). The signals of Mo 3d are divided into Mo $3d_{5/2}$ and Mo $3d_{3/2}$, the characteristic peaks at 229.0 ± 0.1 and 232.1 ± 0.1 eV are attributed to Mo^{4+} species in MoS_2 phases, and the characteristic peaks at 232.5 ± 0.1 and 235.6 ± 0.1 eV are considered as Mo^{6+} species. From the statistical data in the Table 4, that NiMo/TD-70 catalyst has the highest sulfur degree of 74%, which are beneficial to the formation of "Ni-Mo-S-II" phase and the improvement of HDS performance of various catalysts (Liu et al., 2023; Yan et al., 2023).

3.5. Catalytic activity evaluation and reaction network analysis

Figs. 11 and 12 show the DBT and 4,6-DMDBT HDS performance of NiMo/TD-*x* series catalysts. With the decrease of weight hourly space velocities (WHSV = 100–10 h^{-1}), the DBT and 4,6-DMDBT conversion increases due to more complete reaction. With the aging temperature increases, the HDS activity of series catalysts increases gradually at first and then decreases. NiMo/TD-70 shows the highest DBT HDS activity (99.0%) and 4,6-DMDBT HDS activity (93.7%) compared with other catalysts and commercial $NiMo/Al_2O_3$ catalyst, which could be attributed to its appropriate three-dimensional channel structure and ordered pore distribution, which can be conducive to eliminate the influence of steric hindrance of reactants. Additionally, its excellent HDS performance also benefits from the highest sulfurization degree of MoS_2, contributing more active sites to adsorb more S atoms. Compared with DBT, the conversation of 4,6-DMDBT decreases at different WHSV (100–10 h^{-1}), suggesting that the methyl substituent have

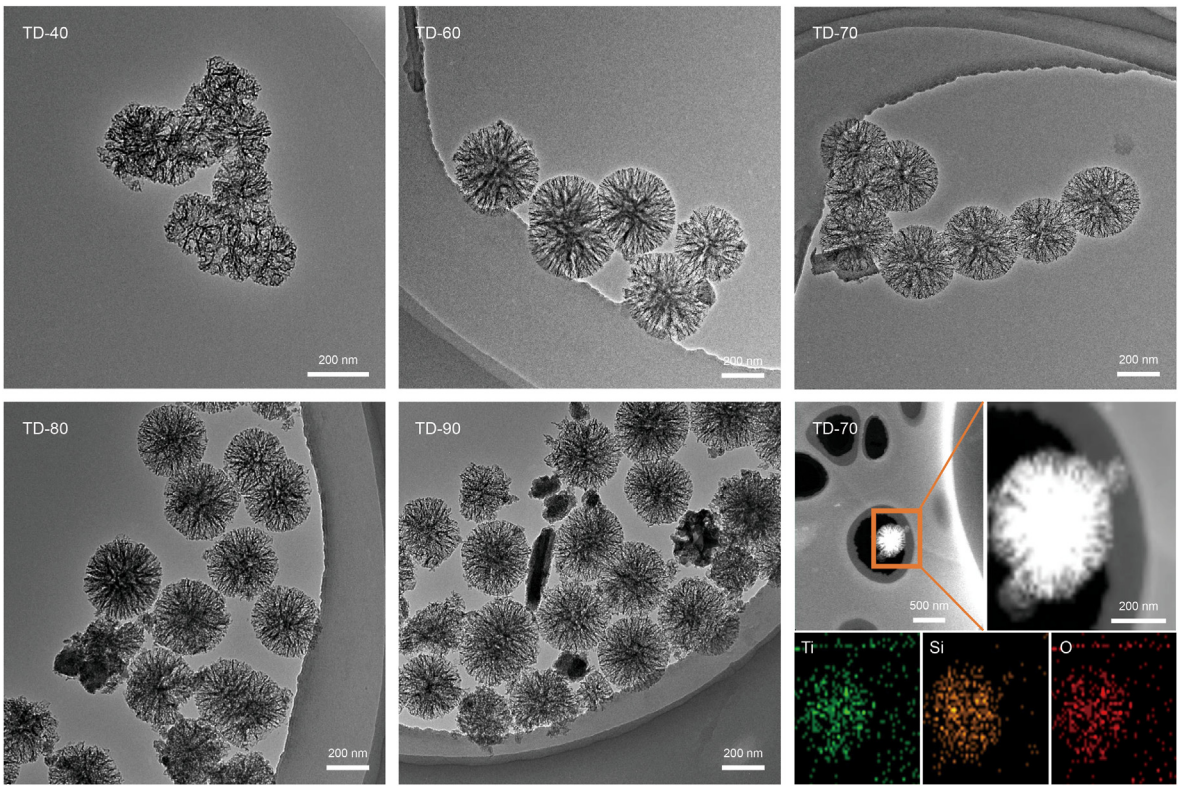

Fig. 6. TEM of TD-*x* supports and HAADF-STEM and EDS images of TD-70 support.

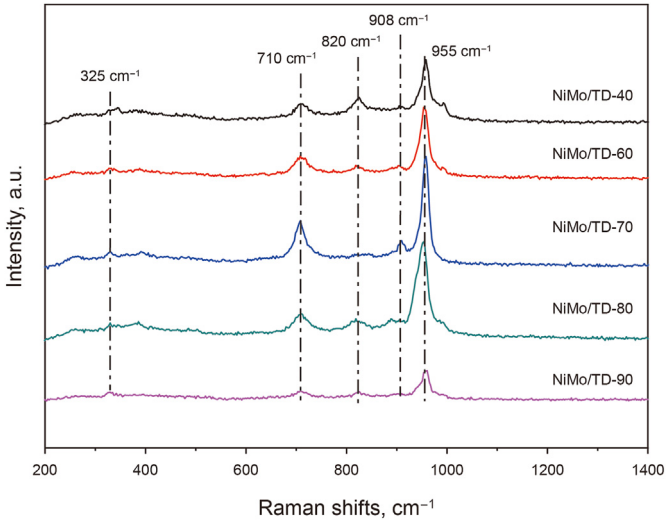

Fig. 7. Raman spectra of the oxide catalysts.

steric hindrance effect, thus hindering the direct desulfurization reaction of 4,6-DMDBT. Meanwhile, the NiMo/TD-70 catalyst exhibits good catalyst stability (Fig. S4).

The distribution of products and the reaction network over NiMo/TD-*x* series catalysts are analyzed by GC-MS and the final results are listed in Table 5 and Table 6.

(i) The DBT HDS reaction mechanism are presented in Fig. 13. HDS reaction mainly includes HYD and DDS routes. In DDS route, the C–S bonds break directly to obtain the principle product biphenyl (BP). As for the HYD process, tetrahydrodibenzothiophene (THDBT) is first generated via hydrogenation of the benzene ring, and further desulfurized to generate cyclohexenylbenzene (CHEB). A small amount of ISO products is found over NiMo/TD-*x* series catalysts. According to Table 5, it can be found that BP accounts for the largest proportion in the products over series catalysts and the ratios of HYD/DDS changes in the sequence of NiMo/TD-70>NiMo/TD-80>NiMo/TD-60>NiMo/TD-40>NiMo/TD-90, illustrating that the DDS path of NiMo/TD-70 catalyst present highest HYD/DDS ratio among NiMo/TD-*x* series catalysts. Besides, the rate constants (k_{HDS}) and the turnover frequency (TOF) values of NiMo/TD-*x* series catalysts also follow the same sequence as the HYD/DDS ratios and NiMo/TD-70 possesses the highest k_{HDS} (12.8×10^{-4} mol g^{-1} s^{-1}) and TOF ($3.1\ h^{-1}$).

(ii) To explore the process of 4,6-DMDBT HDS reaction, Fig. 14 shows the possible reaction network. There are three paths: DDS, HYD and ISO paths. Especially, the ISO path is a typical process, two methyl substituents are first alkyl isomerized into 3,7-DMDBT or 2,8-DMDBT with small steric hindrance, and then conduct deep HDS reaction along the HYD and DDS paths. The change rule of total ISO paths as well as the related k_{HDS} and TOF values is consistent with DBT

4. Discussion

A series of micro-mesoporous composites and the corresponding NiMo/TD-*x* catalysts are designed HDS reactions. NiMo/TD-70 with typical dendritic morphology, strong acidity and suitable MSI displays the optimum DBT and 4,6-DMDBT HDS activity. Based on the above research, detailed analysis of structure-activity

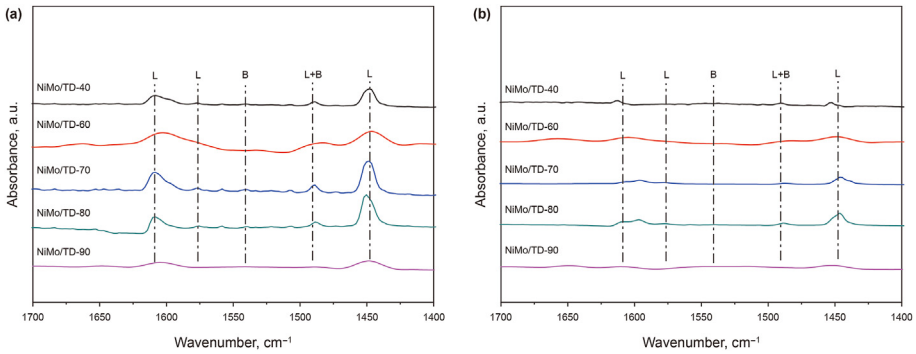

Fig. 8. Py-FTIR spectra of the series NiMo/TD-*x* catalysts after degassing at 200 °C (**a**) and 350 °C (**b**).

Table 2
The amounts of acid determined by Py-FTIR of NiMo/TD-*x* catalysts.

Catalysts	Amount of acid sites, μmol g^{-1}							
	200 °C				350 °C			
	L	B	L + B	B/L	L	B	L + B	B/L
NiMo/TD-40	62.6	0.9	63.5	0.01	11.4	0	11.4	0
NiMo/TD-60	85.1	1.6	86.7	0.02	33.0	0	33.0	0
NiMo/TD-70	107.0	4.3	111.3	0.04	24.7	0	24.7	0
NiMo/TD-80	100.0	2.8	102.8	0.03	36.2	0	36.2	0
NiMo/TD-90	52.5	1.3	53.8	0.02	15.3	0	15.3	0

Table 3
L_{av} and S_{av} of MoS_2 crystallites.

Catalyst	L_{av}, nm	S_{av}	f_{Mo}
NiMo/TD-40	4.12	3.09	0.25
NiMo/TD-60	4.08	3.08	0.26
NiMo/TD-70	3.66	3.05	0.28
NiMo/TD-80	3.82	3.19	0.26
NiMo/TD-90	4.29	2.97	0.24

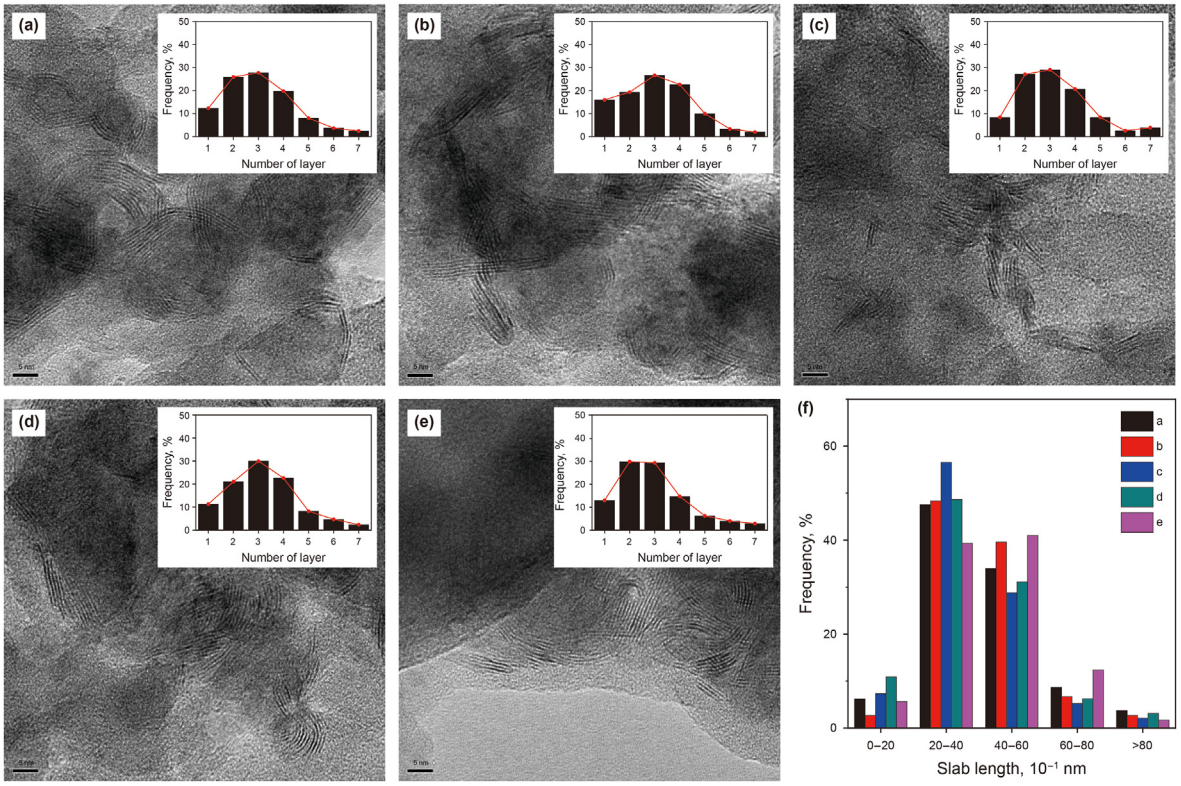

Fig. 9. HRTEM of the sulfide catalysts (**a**) NiMo/TD-40, (**b**) NiMo/TD-60, (**c**) NiMo/TD-70, (**d**) NiMo/TD-80, (**e**) NiMo/TD-90.

relationship is listed as follows:

(1) TD-70 support possesses the special three-dimensional dendritic morphology, wrinkled surface and outstanding pore structures, promoting the dispersion of the NiMo active metal and devoting to the diffusion of macromolecular S-containing compounds. TD-70 support has a large specific surface, pore volume and pore diameter (Fig. 4 and Table 1),

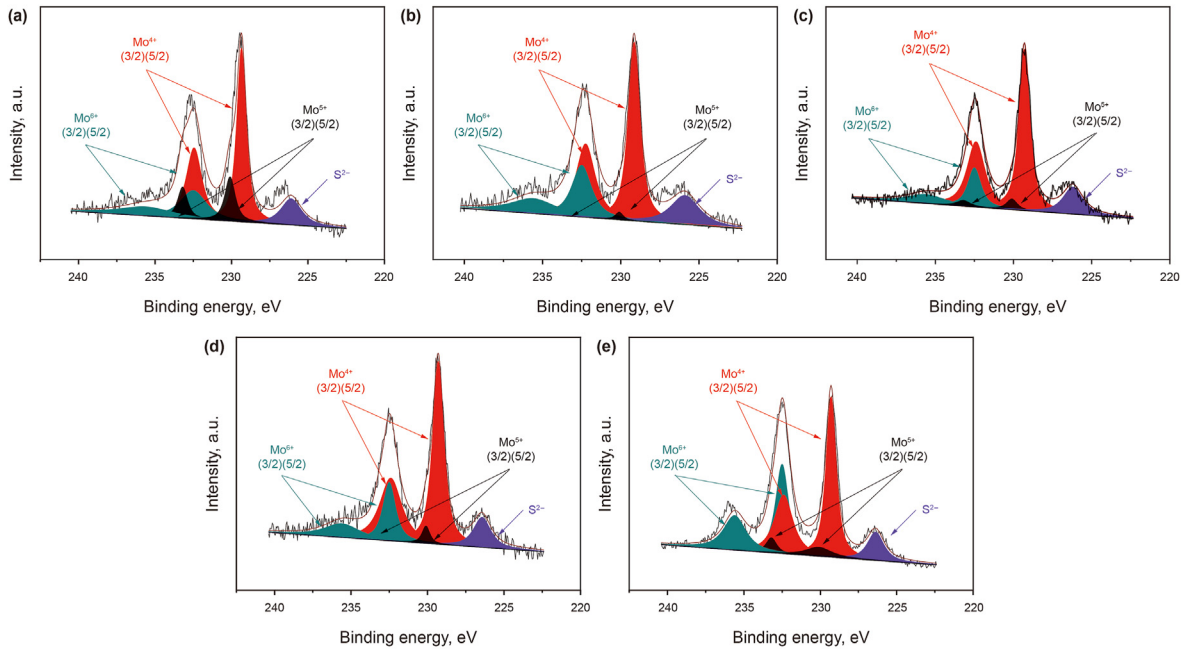

Fig. 10. XPS of the Mo 3d region of the sulfide catalysts, (**a**) NiMo/TD-40, (**b**) NiMo/TD-60, (**c**) NiMo/TD-70, (**d**) NiMo/TD-80, (**e**) NiMo/TD-90.

Table 4
The Mo 3d XPS analysis results of Mo species over various sulfide catalysts.

Catalysts	Mo^{4+}		Mo^{5+}		Mo^{6+}		S_{Mo}
	ar, %[a] (229.0 eV)	*ar*, % (232.1 eV)	*ar*, % (230.1 eV)	*ar*, % (233.2 eV)	*ar*, % (232.5 eV)	*ar*, % (235.6 eV)	
NiMo/TD-40	35	23	10	6	16	10	58
NiMo/TD-60	40	26	1	1	19	13	66
NiMo/TD-70	45	29	3	2	12	9	74
NiMo/TD-80	42	28	3	2	15	10	70
NiMo/TD-90	32	22	5	3	23	15	54

[a] *ar*. % means the area percent of XPS peak.

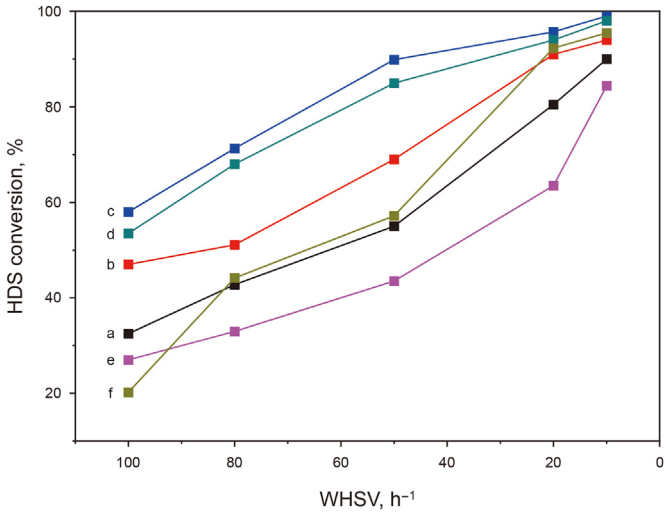

Fig. 11. HDS results of DBT over catalysts at different WHSVs, a, NiMo/TD-40, b, NiMo/TD-60, c, NiMo/TD-70, d, NiMo/TD-80, e, NiMo/TD-90, f, $NiMo/Al_2O_3$.

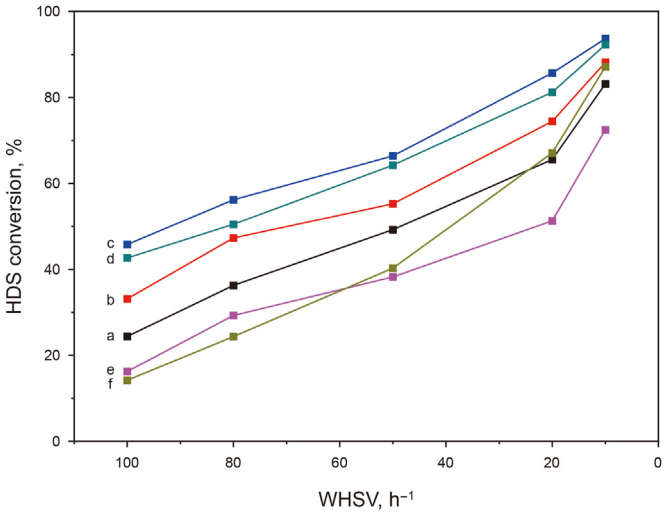

Fig. 12. HDS results of 4,6-DMDBT over catalysts at different WHSVs, a, NiMo/TD-40, b, NiMo/TD-60, c, NiMo/TD-70, d, NiMo/TD-80, e, NiMo/TD-90, f, $NiMo/Al_2O_3$.

which is favor to improving the accessibility of active phases and eliminating the steric resistance of 4,6-DMDBT.

(2) The enhancement of B (L) acid is helpful to improve the activity of HDS reaction. Significantly, the acidity of NiMo/TD-*x* catalysts change greatly due to the modulation of aging

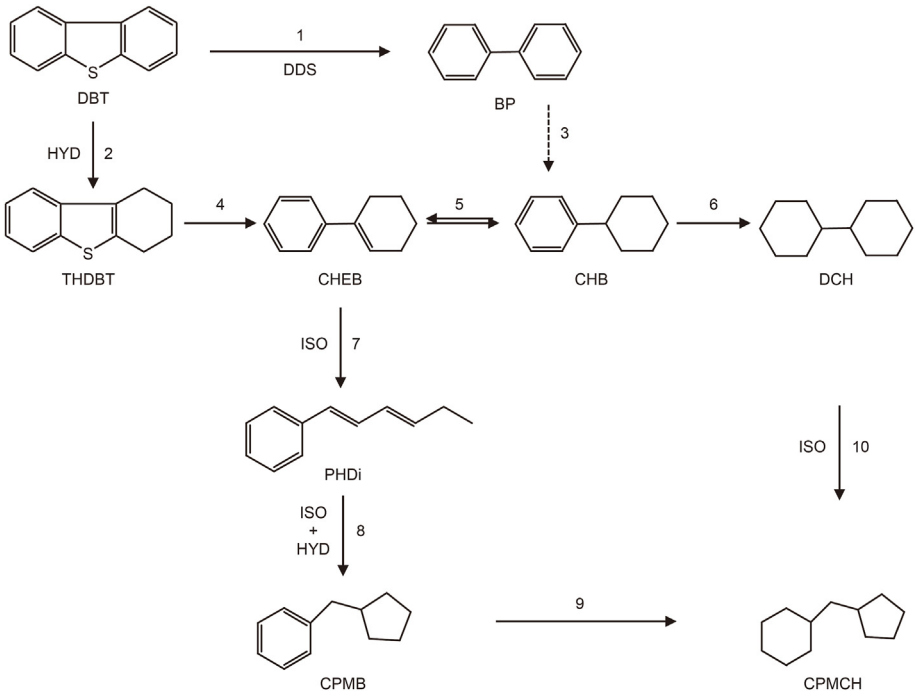

Fig. 13. Reaction network of DBT HDS over the NiMo/TD series catalysts.

Table 5
Catalytic performance for HDS of DBT over different catalysts.

Catalyst	$k_{HDS,}$ 10^{-4} mol g^{-1} h^{-1}	TOF, h^{-1}	Product selectivity, %							
			HYD						DDS	HYD/DDS ratio
			THDBT	CHB	DCH	CPMB	PHDi	CPMCH	BP	
NiMo/TD-40	6.6	1.8	3.3	21.8	1.3	0.4	–	0.3	72.9	0.37
NiMo/TD-60	9.3	2.4	1.8	27.0	1.6	0.4	–	0.4	68.8	0.45
NiMo/TD-70	12.8	3.1	2.6	33.8	2.2	1.1	0.2	1.3	58.8	0.70
NiMo/TD-80	11.5	2.8	1.2	32.1	1.8	0.7	–	0.8	63.4	0.58
NiMo/TD-90	4.4	1.2	1.8	11.0	0.4	0.1	–	–	86.7	0.15

Table 6
Catalytic performance for HDS of 4,6-DMDBT over different catalysts.

Catalyst	$k_{HDS,}10^{-4}$ mol g^{-1} h^{-1}	TOF, h^{-1}	Product selectivity, %							
			HYD			DDS	ISO			Total ISO
			4,6-THDM DBT	3,3′-DM CHB	3,3′-DM BCH	3,3′-DM BP	4,4′-DM BP	4,4′-DM BCH	Iso-MIPT	
NiMo/TD-40	5.4	1.4	13.1	52.5	1.3	14.6	6.9	4.3	7.3	18.5
NiMo/TD-60	7.8	2.0	14.5	49.7	1.3	15.6	8.7	2.9	7.3	18.9
NiMo/TD-70	9.9	2.4	10.9	45.3	3.7	17.1	8.4	4.4	9.1	21.9
NiMo/TD-80	8.9	2.3	10.6	47.3	3.4	17.0	8.0	4.5	9.2	21.7
NiMo/TD-90	2.6	0.7	11.9	50.4	6.0	13.0	5.3	9.1	4.3	18.7

temperatures. The increase of DBT HDS activity over series catalysts is consistent with the increase of B&L acid. NiMo/TD-70 shows the highest DBT conversion due to the moderate acid strength and an appropriate acid-type (Fig. 8 and Table 2), suggesting that the acidic sites promote the reaction. It is also noted that the 4,6-DMDBT HDS activity changes as well as DBT. Moreover, Rich acid content (especially B acid) can improve the hydrogenolysis and isomerization abilities. NiMo/TD-70 shows the highest 4,6-DMDBT conversion with highest ISO reaction.

(3) The MSI of the catalysts will affect the dispersion and reduction of active components, thus affecting HDS reaction activity. From Raman and XPS results (Figs. 7 and 10), it can be found that the agglomerated MoO_3 species are non-existent in all of the catalysts. The change of aging temperatures can adjust the MSI, thus affecting the existing state and dispersion of the NiMo active phase. NiMo/TD-70 catalyst has the highest sulfurization degree (74%) (Fig. 10 and Table 4), the shortest length (3.66 nm), moderate staking layers (3.05) and the highest dispersion degree (0.28) of

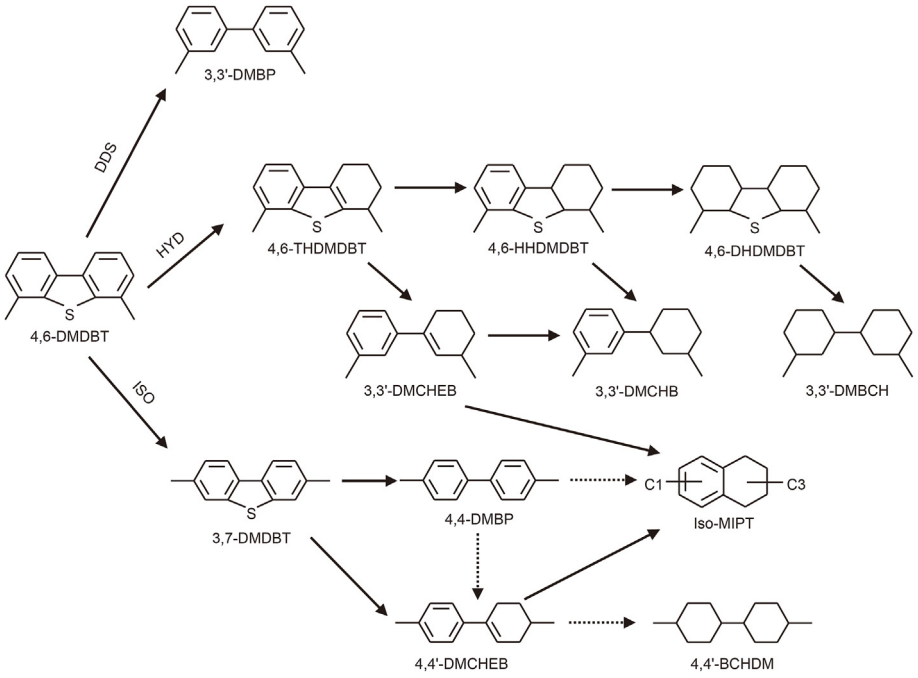

Fig. 14. Reaction network of 4,6-DMDBT HDS over the NiMo/TD series catalysts.

MoS_2 (Fig. 9 and Table 3), thus improving the k_{HDS} and TOF of DBT and 4,6-DMDBT HDS (Tables 5 and 6).

To sum up, this study shows that the synergistic effect of morphology, structure, acidity and active metal dispersion on HDS activity of NiMo/TD-*x* series catalysts. The open center-radial pore structure can provide more reaction space for macromolecular reactants. Active metals are more evenly distributed on the supports, mainly due to the larger specific surface areas and pore volumes and suitable MSI. The typical dendritic morphology, largest surface, more B&L acid sites and outstanding dispersion of active metals over NiMo/TD-70 are conducive to the hydrogenation and isomerization of DBT and 4,6-DMDBT molecules.

5. Conclusion

NiMo/TD-*x* series catalysts with different morphologies and acidity are synthesized by a facile method. TS-1 microporous material will not damage the fold topology of DMSNs, and can be well composited to the framework of DMSNs via Si—O—Ti bonds. NiMo/TD-70 catalyst has typical wrinkled surface dendritic morphology and outstanding pore structures, promoting the dispersion of the NiMo active metal. Moreover, the introduction of TS-1 brings more B&L acid sites, promoting the HYD selectivity for DBT and the ISO route for 4,6-DMDBT. Obviously, NiMo/TD-70 catalyst shows the highest k_{HDS} and TOF values, which mean the excellent DBT (99.0%) and 4,6-DMDBT (93.7%) activity.

Declaration of competing interest

The authors declare that they have no known competing financial interests or personal relationships that could have appeared to influence the work reported in this paper.

Acknowledgment

This research was supported by the Science Foundation of China University of Petroleum-Beijing (No. 2462023QNXZ002), the National Key R&D Program of China (2021YFA1501201), the National Natural Science Foundation of China (No.22278174), Independent research project of State Key Laboratory of heavy oil (2021—01) and Shandong Excellent Young Scientists Fund Program (Overseas, 2022HWYQ-082).

Appendix A. Supplementary data

Supplementary data to this article can be found online at https://doi.org/10.1016/j.petsci.2023.07.004.

References

Badoga, S., Mouli, C.K., Soni, K.K., et al., 2012. Beneficial influence of EDTA on the structure and catalytic properties of sulfided NiMo/SBA-15 catalysts for hydrotreating of light gas oil. Appl. Catal. B Environ. 125, 67—84. https://doi.org/10.1016/j.apcatb.2012.05.015.

Bouwens, S.S., Zon, V., Dijk, V.M., et al., 1994. On the structural differences between alumina-supported comos type I and alumina-, silica-, and carbon-supported comos type II phases studied by XAFS, MES, and XPS. J. Catal. 146 (2), 375—393. https://doi.org/10.1006/jcat.1994.1076.

Du, S.T., Sun, Q.M., Wang, N., et al., 2017. Synthesis of hierarchical TS-1 zeolites with abundant and uniform intracrystalline mesopores and their highly efficient catalytic performance for oxidation desulfurization. J. Mater. Chem. 5 (17), 7992—7998. https://doi.org/10.1039/C6TA10044A.

Duan, A., Li, T., Zhen, Z., et al., 2015a. Synthesis of hierarchically porous L-KIT-6 silica—alumina material and the super catalytic performances for hydrodesulfurization of benzothiophene. Appl. Catal. B Environ. 165, 763—773. https://doi.org/10.1016/j.apcatb.2014.10.078.

Duan, A., Li, T., Niu, H., et al., 2015b. Synthesis of a novel zeolite W and application in the catalyst for FCC gasoline hydro-upgrading. Catal. Today 245, 163—171. https://doi.org/10.1016/j.cattod.2014.05.030.

Haandel, L.V., Bremmer, M., Kooyman, P.J., et al., 2015. Structure-activity correlations in hydrodesulfurization reactions over Ni-promoted $Mo_xW_{(1-x)}S_2/Al_2O_3$ catalysts. ACS Catal. 5 (12), 7276—7287. https://doi.org/10.1021/acscatal.5b01806.

Hamdy, M.S., Berg, O., Jansen, J.C., et al., 2010. TiO_2 nanoparticles in mesoporous TUD-1: synthesis, characterization and photocatalytic performance in propane oxidation. Chemistry 12 (2), 620—628. https://doi.org/10.1002/chem.200500649.

Han, W., Nie, H., Long, X.Y., et al., 2016. Preparation of F-doped MoS_2/Al_2O_3 catalysts as a way to understand the electronic effects of the support Brønsted acidity on HDN activity. J. Catal. 339, 135—142. https://doi.org/10.1016/j.jcat.2016.04.005.

Ho, T.C., Mcconnachie, J.M., 2011. Ultra-deep hydrodesulfurization on MoS_2 and $Co_{0.1}MoS_2$: intrinsic vs. environmental factors. J. Catal. 277 (1), 117–122. https://doi.org/10.1016/j.jcat.2010.10.017.

Hu, D., Li, H.P., Mei, J.L., et al., 2020. Ultrasmall particle sizes of walnut-like mesoporous silica nanospheres with unique large pores and tunable acidity for hydrogenating reaction. Small 16 (29), 2002091–2002099. https://doi.org/10.1002/smll.202002091.

Huang, X., Tao, Z., Praskavich, J.C., et al., 2014. Dendritic silica nanomaterials (KCC-1) with fibrous pore structure possess high DNA adsorption capacity and effectively deliver genes in vitro. Langmuir the Acs Journal of Surfaces & Colloids 30 (36), 10886–10898. https://doi.org/10.1021/la501435a.

Lee, W.S., Zhang, R., Akatay, M.C., et al., 2011. Differences in catalytic sites for CO oxidation and propylene epoxidation on Au nanoparticles. ACS Catal. 1 (10), 1327–1330. https://doi.org/10.1021/cs200373f.

Lei, Y., Xiang, L., Wang, A., et al., 2015. Hydrodesulfurization of dibenzothiophene, 4,6-dimethyldibenzothiophene, and their hydrogenated intermediates over bulk tungsten phosphide. J. Catal. 330, 330–343. https://doi.org/10.1016/j.jcat.2015.07.019.

Lei, Z., Fu, W., Ke, Q., et al., 2012. Study of hydrodesulfurization of 4,6-DMDBT over Pd supported on mesoporous USY zeolite. Applied Catalysis A General 433–434, 251–257. https://doi.org/10.1016/j.apcata.2012.05.028.

Li, J.C., Li, J.M., Zhao, Z., et al., 2017. Size effect of TS-1 supports on the catalytic performance of PtSn/TS-1 catalysts for propane dehydrogenation. J. Catal. 352, 361–370. https://doi.org/10.1016/j.jcat.2017.05.024.

Li, Y., Chi, K., Zhang, H., et al., 2018. The influence of hydrothermal crystallization temperature on a novel FDU-12 mesoporous composite assembled by ZSM-5 nanoclusters and its hydrodesulfurization performance for DBT and FCC diesel. Fuel Process. Technol. 180, 56–66. https://doi.org/10.1016/j.fuproc.2018.08.010.

Liang, J., Wu, M., Wei, P., et al., 2018. Efficient hydrodesulfurization catalysts derived from Strandberg PMoNi polyoxometalates. J. Catal. 358, 155–167. https://doi.org/10.1016/j.jcat.2017.11.026.

Liu, C., Mei, J.L., Wang, G., et al., 2020. Tailoring NiMoS active phases with high hydrodesulfurization activity through facilely synthesized supports with tunable mesostructure and morphology. J. Catal. 387, 170–185. https://doi.org/10.1016/j.jcat.2020.04.012.

Liu, J.X., Liu, X.Q., Yan, R.X., et al., 2023. Active phase morphology engineering of $NiMo/Al_2O_3$ through La introduction for boosting hydrodesulfurization of 4, 6-DMDBT. Petrol. Sci. 20 (2), 1231–1237. https://doi.org/10.1016/j.petsci.2022.09.023.

Ma, R., Guo, J., Wang, D., et al., 2019. Preparation of highly dispersed WO_3/few layer g-C_3N_4 and its enhancement of catalytic oxidative desulfurization activity. Colloids and Surf. A Physicochem. Eng. Aspect. 572, 250–258. https://doi.org/10.1016/j.colsurfa.2019.04.006.

Mestl, G., Srinivasan, T., 1998. Raman spectroscopy of monolayer-type oxide catalysts: supported Mo oxides. Catalysis Reviews. Sci. Eng. 40 (4), 451–570. https://doi.org/10.1080/01614949808007114.

Moliner, M., Martínez, C., Corma, A., 2015. Multipore zeolites: synthesis and catalytic applications. Angew. Chem. Int. Ed. 54, 3560–3579. https://doi.org/10.1002/anie.201406344.

Nikolla, E., Yuriy, R.L., Moliner, M., et al., 2011. "One-Pot" synthesis of 5-(hydroxymethyl)furfural from carbohydrates using tin-beta zeolite. ACS Catal. 1 (4), 408–410. https://doi.org/10.1021/cs2000544.

Parola, V.L., Deganello, G., Tewell, C.R., et al., 2002. Structural characterisation of silica supported CoMo catalysts by UV Raman spectroscopy, XPS and X-ray diffraction techniques. Applied Catalysis A General 235 (1), 171–180. https://doi.org/10.1016/S0926-860X(02)00261-2.

Prins, R., De Beer, V.H.J., Somorjai, G.A., 1989. Structure and function of the catalyst and the promoter in Co-Mo hydrodesulfurization catalysts. Catal. Rev. 31 (1–2), 1–41. https://doi.org/10.1080/01614948909351347.

Salerno, P., Mendioroz, S., Agudo, A.L., 2004. Al-pillared montmorillonite-based NiMo catalysts for HDS and HDN of gas oil: influence of the method and order of Mo and Ni impregnation. Applied Catalysis A General 259 (1), 17–28. https://doi.org/10.1016/j.apcata.2003.09.019.

Shan, S., Pei, Y., Wei, H., et al., 2015. Supported NiW catalysts with tunable size and morphology of active phases for highly selective hydrodesulfurization of fluid catalytic cracking naphtha. J. Catal. 330, 288–301. https://doi.org/10.1016/j.jcat.2015.06.019.

Shen, D., Yang, J., Li, X., et al., 2014. Biphase stratification approach to three-dimensional dendritic biodegradable mesoporous silica nanospheres. Nano Lett. 14 (2), 923–932. https://doi.org/10.1021/nl404316v.

Shan, S.F., Liu, H.Y., Yue, Y.Y., et al., 2016. Trimetallic WMoNi diesel ultra-deep hydrodesulfurization catalysts with enhanced synergism prepared from inorganic-organic hybrid nanocrystals. J. Catal. 344, 325–333. https://doi.org/10.1016/j.jcat.2016.09.019.

Song, H., Wang, J., Wang, Z., et al., 2014. Effect of titanium content on dibenzothiophene HDS performance over Ni_2P/Ti-MCM-41 catalyst. J. Catal. 311, 257–265. https://doi.org/10.1016/j.jcat.2013.11.021.

Sun, J., Bonneau, C., Cantin, A., et al., 2009. The ITQ-37 mesoporous chiral zeolite. Nature 458 (7242), 1154–1157. https://doi.org/10.1038/nature07957.

Wang, X.L., Du, P., Chi, K.B., et al., 2017a. Synthesis of NiMo catalysts supported on mesoporous silica FDU-12 with different morphologies and their catalytic performance of DBT HDS. Catal. Today 291, 146–152. https://doi.org/10.1016/j.cattod.2016.10.035.

Wang, X.L., Xiao, C.K., Mei, J.L., et al., 2020a. Structural screening and design of dendritic micro-mesoporous composites for efficient hydrodesulfurization of dibenzothiophene and 4,6-dimethyldibenzothiophene. ACS Appl. Mater. Interfaces 12 (36), 40404–40414. https://doi.org/10.1021/acsami.0c12631.

Wang, X.L., Li, Y., Chi, K.B., et al., 2018a. Optimal synthesis of hierarchical porous composite ZSM-5/SBA-16 for ultradeep hydrodesulfurization of dibenzothiophene and 4,6- dimethyldibenzothiophene. part 1: the influence of inorganic salt on the properties of NiMo catalysts. Energy Fuel. 32 (5), 6204–6212. https://doi.org/10.1021/acs.energyfuels.8b00708.

Wang, X.L., Xiao, C.K., Zheng, P., et al., 2020b. Dendritic micro–mesoporous composites with center-radial pores assembled by TS-1 nanocrystals to enhance hydrodesulfurization activity of dibenzothiophene and 4,6-dimethyldibenzothiophene. J. Catal. 384, 136–146. https://doi.org/10.1016/j.jcat.2020.02.013.

Wang, X.L., Zhao, Z., Chen, Z.T., et al., 2017. Effect of synthesis temperature on structure-activity-relationship over $NiMo/\gamma$-Al_2O_3 catalysts for the hydrodesulfurization of DBT and 4,6-DMDBT. Fuel Process. Technol. 161, 52–61. https://doi.org/10.1016/j.fuproc.2017.03.003.

Wang, X.L., Zhao, Z., Zheng, P., et al., 2016. Synthesis of NiMo catalysts supported on mesoporous Al_2O_3 with different crystal forms and superior catalytic performance for the hydrodesulfurization of dibenzothiophene and 4,6-dimethyldibenzothiophene. J. Catal. 34, 680–691. https://doi.org/10.1016/j.jcat.2016.10.016.

Wang, X.L., Mei, J.L., Zhao, Z., et al., 2018b. Self-assembly of hierarchically porous ZSM-5/SBA-16 with different morphologies and its high isomerization performance for hydrodesulfurization of dibenzothiophene and 4,6-dimethyldibenzothiophene. ACS Catal. 8 (3), 1891–1902. https://doi.org/10.1021/acscatal.7b04147.

Wu, H.D., Duan, A.J., Zhao, Z., et al., 2014. Synthesis of NiMo hydrodesulfurization catalyst supported on a composite of nano-sized ZSM-5 zeolite enwrapped with mesoporous KIT-6 material and its high isomerization selectivity. J. Catal. 317, 303–317. https://doi.org/10.1016/j.jcat.2014.07.002.

Wu, S.H., Hung, Y., Mou, C.Y., 2011. Mesoporous silica nanoparticles as nanocarriers. Chem. Commun. 47 (36), 9972–9985. https://doi.org/10.1039/C1CC11760B.

Xiao, C.K., Xia, Z.S., Chi, K.B., et al., 2018. Titanium modified TUD-1 mesoporous catalysts for hydrotreating of FCC diesel. Energy Fuel. 32 (8), 8210–8219. https://doi.org/10.1021/acs.energyfuels.8b01543.

Xiao, C.K., Song, S.T., Zou, Y.T., et al., 2021. Facile synthesis of few-layer MoS_2 nanosheets with different morphologies supported on Al-TUD-1 for efficient hydrodesulfurization of dibenzothiophene and 4,6-dimethyldibenzothiophene. Chem. Eng. J. 425, 131416. https://doi.org/10.1016/j.cej.2021.131416.

Yan, R.X., Liu, X.Q., Liu, J.X., et al., 2023. Modulating the active phase structure of $NiMo/Al_2O_3$ by La modification for ultra-deep hydrodesulfurization of diesel. AIChE J. 69 (2), e17873. https://doi.org/10.1002/aic.17873.

Yu, Y.J., Xing, J.L., Pang, J.L., et al., 2014. Facile synthesis of size controllable dendritic mesoporous silica nanoparticles. ACS Appl. Mater. Interfaces 6 (24), 22655–22665. https://doi.org/10.1021/am506653n.

Zhang, D.Q., Duan, A.J., Zhao, Z., et al., 2010. Synthesis, characterization, and catalytic performance of NiMo catalysts supported on hierarchically porous Beta-KIT-6 material in the hydrodesulfurization of dibenzothiophene. J. Catal. 274 (2), 273–286. https://doi.org/10.1016/j.jcat.2010.07.012.

Zhao, L., Yu, J.G., 2006. Controlled synthesis of highly dispersed TiO_2 nanoparticles using SBA-15 as hard template. J. Colloid Interface Sci. 304 (1), 84–91. https://doi.org/10.1016/j.jcis.2006.08.042.

Zhou, W.W., Liu, M.F., Zhang, Q., et al., 2017. Synthesis of NiMo catalysts supported on gallium containing mesoporous Y zeolites with different gallium contents and their high activities in the hydrodesulfurization of 4,6-dimethyldibenzothiophene. ACS Catal. 7 (11), 7655–7679. https://doi.org/10.1021/acscatal.7b02705.

Zhou, W.W., Wei, Q., Zhou, Y.S., et al., 2018. Hydrodesulfurization of 4,6-dimethyldibenzothiophene over NiMo sulfide catalysts supported on meso-microporous Y zeolite with different mesopore sizes. Appl. Catal. B Environ. 238, 212–224. https://doi.org/10.1016/j.apcatb.2018.07.042.

Zhou, X.F., Zhao, Z., Duan, A.J., 2014. Synthesis of hierarchically porous silicas with mesophase transformations in a four-component microemulsion-type system and the catalytic performance for dibenzothiophene hydrodesulfurization. J. Mater. Chem. 2 (19), 6823–6833. https://doi.org/10.1039/C3TA14859A.